AGU PUBLICATIONS

JGR

Journal of Geophysical Research: Solid Earth

RESEARCH ARTICLE

10.1002/2016JB013681

Key Points:

- Slow and fast slip events are generated on a 760 mm long granite laboratory fault; slow events produce swarms of tiny (M −6) seismic events
- Abrupt increases in loading rate and long healing periods can shrink the spatial and temporal extent of the nucleation zone
- Seismic coupling coefficient is constant for slip rates above 70 mm/s and decreases with decreasing slip velocity below 70 mm/s

Supporting Information:

- Supporting Information S1

Correspondence to:
G. C. Mclaskey,
gcm8@cornell.edu

Citation:
Mclaskey, G. C., and F. Yamashita (2017), Slow and fast ruptures on a laboratory fault controlled by loading characteristics, *J. Geophys. Res. Solid Earth*, *122*, doi:10.1002/2016JB013681.

Received 25 OCT 2016
Accepted 18 APR 2017
Accepted article online 24 APR 2017

Slow and fast ruptures on a laboratory fault controlled by loading characteristics

Gregory C. Mclaskey[1] and Futoshi Yamashita[2]

[1]School of Civil and Environmental Engineering, Cornell University, Ithaca, New York, USA, [2]National Research Institute for Earth Science and Disaster Resilience, Tsukuba, Japan

Abstract Recent geodetic observations indicate that a single fault may slip slowly and silently or fast and seismically in different circumstances. We report laboratory experiments that demonstrate how the mode of faulting can alternate between fast "stick-slip" events (70 to ~500 mm/s sliding rates) and slow silent events (~0.001 to 30 mm/s) as a result of loading conditions rather than friction properties or stiffness of the loading machine. The 760 mm long granite sample is close to the critical nucleation length scale for unstable slip, so small variations in nucleation properties result in measurable differences in slip events. Slow events occur when instability cannot fully nucleate before reaching the sample ends. Dynamic events occur after long healing times or abrupt increases in loading rate which suggests that these factors shrink the spatial and temporal extents of the nucleation zone. Arrays of slip, strain, and ground motion sensors installed on the sample allow us to quantify seismic coupling and study details of premonitory slip and afterslip. We find that seismic coupling decreases when slip rates fall below about 70 mm/s. The slow slip events we observe are primarily aseismic (less than 1% of the seismic coupling of faster events) and produce swarms of very small M −6 to M −8 events. These mechanical and seismic interactions suggest that faults with transitional behavior—where creep, small earthquakes, and tremor are often observed—could become seismically coupled if loaded rapidly, either by a slow slip front or dynamic rupture of an earthquake that nucleated elsewhere.

Plain Language Summary Some faults slip slowly and silently, while others are locked and then slip spontaneously and generate destructive earthquakes. Recent observations show that a single fault may slip in either mode under different circumstances. We have conducted laboratory earthquake experiments where we force a fault cut in a 760 mm long granite rock to slip, similar to the way a natural fault slips in an earthquake. The experiments demonstrate that the same rock sample will either slip rapidly or slowly based on how quickly we apply force to it and how long we let the rock rest in between successive laboratory earthquakes. When the rock slips rapidly (70 to ~500 mm/s), it generates vibrations that are similar to a magnitude −3 earthquake. When the rock slips slowly (~0.001 to 30 mm/s), most of the slip occurs silently. The vibrations that the slowly sliding rock does produce are a swarm of tiny earthquakes with magnitudes ranging from −6 down to at least −8 detected with instruments sensitive to nanometer-scale displacements. Studying fault slip and vibrations in the laboratory will help us better understand the mechanics of natural earthquakes and other nearly silent tectonic processes that occur within the Earth.

1. Introduction

Faults are often categorized by their stability as either steady state velocity strengthening (VS) or steady state velocity weakening (VW). VS fault sections are strongest when they are forced to slip at higher rates. They often contain clay minerals, tend to slip slowly and steadily (i.e., "creep"), and do not restrengthen or "heal" [e.g., *Carpenter et al.*, 2016; *Ikari et al.*, 2011]. VW faults sections are strongest when locked and become weaker at higher sliding velocities. They are typically composed of quartz, slip unstably, and generate earthquakes with strong shaking. Most natural faults likely contain both VS and VW sections [*Boatwright and Cocco*, 1996], and heterogeneous fault properties have been increasingly called upon to explain the diversity of slip behavior observed in nature. For example, VW fault patches embedded in a VS matrix can explain observations of small repeating earthquake sequences [e.g., *Vidale et al.*, 1994; *Marone et al.*, 1995; *Chen and Lapusta*, 2009]. Similar conditions on a larger scale may be the cause of "seismic asperities" that host characteristic earthquakes [e.g., *Johnson et al.*, 2012]. Combinations of VW and VS fault sections are also required to explain spontaneous slow slip and tremor [e.g., *Ide*, 2014; *Nakata et al.*, 2011], shallow episodic creep events and afterslip [e.g., *Wei et al.*, 2013], and short-scale variability in coseismic slip and afterslip [e.g., *Floyd et al.*, 2016].

A growing number of observations also indicate that creeping and seismic sections of the fault are not entirely mutually exclusive. A single fault might slip either seismically or aseismically in different circumstances. As a salient example, much of the fault that slipped coseismically in the 2011 Tohoku earthquake slipped stably both before and after the *M* 9 earthquake, as inferred from both repeating earthquake sequences [e.g., *Uchida and Matsuzawa*, 2013] and geodetic inversions of afterslip [*Ito et al*., 2013; *Johnson et al*., 2012, 2016; *Perfettini and Avouac*, 2014]. This bimodal character is also observed elsewhere [e.g., *Bürgmann et al*., 2002; *Pritchard and Simons*, 2006; *Bedford et al*., 2013; *Lin et al*., 2013; *Barnhart et al*., 2016] and on deeper fault sections that produce tremor [e.g., *Wech and Bartlow*, 2014]. It is likely responsible for certain unique seismic signatures, such as period doubling [*Shelly*, 2010], that can be used to help constrain numerical models [e.g., *Veedu and Barbot*, 2016]. Better seismic hazard assessment requires insight into bimodal behavior and the conditions that promote a seismogenic fault to slip silently or a creeping fault to undergo rapid, seismic slip. This is closely related to the larger outstanding question of how slow slip events can spontaneously nucleate without becoming fully dynamic. Nucleation of a slip instability requires VW fault behavior, while a VS behavior or some other mechanism must act to quench the instability so that slip never accelerates to a seismogenic speed (~1 m/s).

Most models of bimodal slip behavior fall into two broad categories. In the first, friction is assumed to be strongly affected by slip rate. For example, a VS fault that slips slowly under most conditions may be able to weaken and become unstable at high slip rates due to thermal pressurization [e.g., *Tanikawa and Shimamoto*, 2009; *Rice*, 2006; *Noda and Lapusta*, 2013]. This behavior could explain why dynamic rupture is sometimes able to propagate through fault sections that are also thought to accommodate slow and stable creep. The opposite rate dependence may also be possible. For example, serpentine fault gouge can undergo a transition from VW to VS friction behavior above slip rates of ~10 μm/s [*Kaproth and Marone*, 2013]. This strengthening at high slip rates due to dilatancy-induced pore pressure reduction [e.g., *Segall et al*., 2010] or a similar mechanism could explain the existence of slow slip events (SSEs) in nature.

This paper focuses on a second category of models wherein a fault section exhibits behavior close to a critical point that marks a transition between slow and stable behavior and dynamic slip instability [e.g., *Rice and Ruina*, 1983]. This stability transition, described in section 2, marks a balance between the rate of elastic energy release and the rate of frictional strength loss. Rich behavior that includes slow slip events has been demonstrated numerically [*Gu et al*., 1984; *Rice and Gu*, 1983] and experimentally [*Leeman et al*., 2016; *Tinti et al*., 2016]. Continuous fault models have utilized transitional behavior to describe slow slip events [*Liu and Rice*, 2005, 2007] and both fast and slow ruptures on the same VW fault patch [e.g., *Veedu and Barbot*, 2016; *Chen and Lapusta*, 2009]. Other models showed that interactions between VS and VW fault sections may expand the parameter space over which SSEs can occur, so that rheological parameters need not be finely tuned to produce transitional behavior [*Skarbek et al*., 2012]. We report laboratory experiments involving VS-VW interactions that appear to support that result.

We have designed a rock friction machine that operates close to the stability transition. As we will explain in section 3, the 760 mm length of the VW simulated fault is close to the critical length scale for unstable slip h^*. Slip instabilities will begin to nucleate, but the sample is not large enough to fully support nucleation up to seismic slip speeds. By varying loading conditions, this apparatus can generate both slow slip events (SSEs) and fast stick-slip events, which we refer to as dynamic slip events (DSEs). The SSEs we observe are smooth, silent, have a lower stress drop (<4%), and have slip rates of 10 μm/s to 10 mm/s. DSEs are violent, audible, have a higher stress drop (5–20%), and reach slip velocities of at least 0.1 m/s. The mode of faulting (DSE or SSE) can be dictated either through the rate of applied load or by allowing the fault to heal in stationary contact. We generate sequences of events that switch back and forth between DSEs and SSEs in a single experimental run while normal stress and friction properties are held constant.

Our machine uses a bearing composed of reinforced Teflon sliding against precision ground steel plates. Teflon on steel is known to be VS [*Dieterich and Kilgore*, 1994; *Mokha et al*., 1990]. Thus, experiments always include the interaction between a rock/rock simulated fault that is VW and a Teflon bearing that is VS. Most biaxial or triaxial laboratory rock friction machines require at least two interfaces. Some apparatus designs, such as the double direct shear [e.g., *Dieterich*, 1978; *Karner and Marone*, 2000; *Collettini et al*., 2014], utilize two rock/rock interfaces, while others, including direct shear [e.g., *Togo et al*., 2015] and triaxial [e.g., *Blanpied et al*., 1995] configurations, use Teflon shims, rollers, or some other type of bearing. Motion on these secondary interfaces is typically not measured; bearings are assumed to be frictionless, and both interfaces of the double direct shear are assumed to behave in an identical fashion.

Dilatancy hardening or another type of strongly velocity-dependent friction property is not required to explain the SSEs we observe; nor is it expected on the granite/granite surfaces with minimal gouge (approximately tens of micrometers thick). Instead, when a nucleating slip event grows to the size of the sample, it simply runs out of elastic strain energy. Stress is transferred to the VS Teflon bearing, resulting in a SSE. The VW-VS interactions do not dominate the observed behavior, but they appear to facilitate the generation of SSEs over a wider range of parameters than would occur with only VW.

The spectrum of slip rates under otherwise identical conditions allows us to measure its effect on seismic coupling coefficient. We find that fast events exhibit constant seismic coupling, but when slip rates fall below about 70 mm/s the duration of sliding increases, so slip events do not radiate as strongly at high frequencies. The SSEs we observe are primarily aseismic (less than 1% of the seismic coupling of faster events) and produce swarms of very small M −6 to M −8 events.

The bimodal fault behavior and the dependence of stability and seismic radiation on loading conditions described in this paper have application to tectonic faults that exhibit transitional behavior (partly creeping and partly locked). We find that long healing times followed by abrupt increases in loading rate act to promote seismic instability. Thus, a fault section that creeps aseismically under slow tectonic loading (or is mostly aseismic except for some small repeating earthquakes) could become unstable and seismically coupled if loaded by a dynamic rupture front that nucleated elsewhere [e.g., *Chang et al*., 2012; *Noda and Lapusta*, 2013]. Similarly, relatively rapid loading during the passage of a slow slip front could promote the generation of tremor, even if that fault patch would slip silently under different circumstances. Conversely, short healing times and smoothly decreasing loading rates can promote stable aseismic sliding. This could help explain why stable afterslip can occur on VW fault sections [e.g., *Helmstetter and Shaw*, 2009].

We first present an overview of critical stiffness and critical nucleation length scale. In section 3, we outline a simplified two-slider block model used to help explain the mechanics of the experiments. Section 4 describes the experimental details including the sensors employed to study slip, stress changes, and seismicity. Section 5 describes the scaling of observed slip events and presents a detailed comparison between a DSE and a SSE. The VW-VS interactions and the effects of loading rate, healing time, and normal stress are discussed in section 6.

2. Critical Stiffness and Nucleation Length Scale

In laboratory experiments, stable and unstable slip behavior is controlled by the loading system stiffness k in relation to a critical stiffness k_c [*Ruina*, 1983],

$$k_c = \frac{\sigma_n(b-a)}{D_c}, \tag{1}$$

where σ_n is the normal stress, D_c is a characteristic slip distance, and b and a are Dieterich-Ruina, rate- and state-dependent friction parameters [*Dieterich*, 1979; *Ruina*, 1983; *Gu et al*., 1984; *Marone*, 1998]. If $k > k_c$, the laboratory sample will slide stably. If $k < k_c$, it will produce instabilities commonly called stick-slip events and referred to here as DSEs.

The compliance of the loading system $1/k = 1/k_{\mathrm{sample}} + 1/k_{\mathrm{machine}}$, where $1/k_{\mathrm{machine}}$ is the compliance of the loading machine and $1/k_{\mathrm{sample}}$ is the compliance of the sample. One method of measuring k assumes that the loading piston does not advance during a rapid slip event. In this case,

$$k = \Delta\tau_{\mathrm{mech}}/d \tag{2}$$

where $\Delta\tau_{\mathrm{mech}}$ is the sample average shear stress change and d is the sample average slip on the simulated fault measured from one slip event. All inelastic deformation is assumed to occur on the simulated fault within the measurement d. Alternatively, k can be determined during linear elastic loading from $k = \Delta\tau_{\mathrm{mech}}/x_{\mathrm{LP}}$ where x_{LP} is the load point displacement. This assumes that the sample is locked and x_{LP} includes all inelastic deformation.

Large samples often produce cases where $k_{\mathrm{sample}} < k_{\mathrm{machine}}$ and the critical point can be controlled by the compliance of the sample $k \approx k_{\mathrm{sample}}$, and slip instabilities can nucleate from within the sample

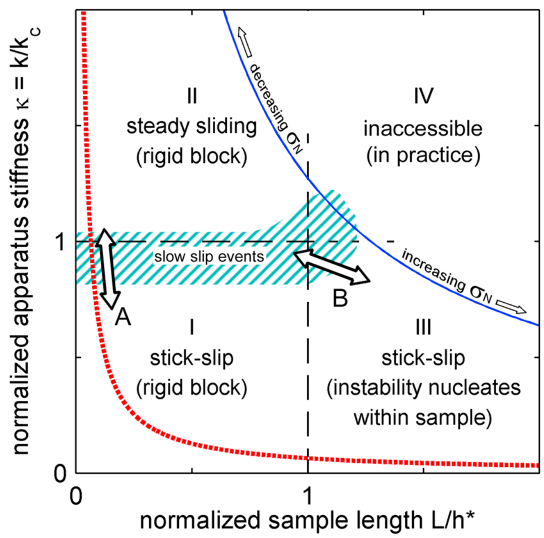

Figure 1. A map of parameter space for the behavior of laboratory experiments is broken into four quadrants based on the shear loading stiffness k relative to a critical stiffness k_c and sample length L relative to a critical length scale h^*. The hashed region indicates slow slip behavior. The blue and red dashed lines show the path through parameter space taken by changing normal stress and keeping all other parameters constant. The red dashed line shows behavior for small stiff samples ($k_{\mathrm{sample}} >> k_{\mathrm{machine}}$), while the blue line maps large compliant samples ($k_{\mathrm{sample}} << k_{\mathrm{machine}}$) (see text). Our experiments likely map near the arrow labeled "B."

independent of the loading apparatus. Taking into account the shear modulus G of the sample, a critical nucleation length scale can be defined [*Dieterich*, 1992]

$$h^* = \frac{G}{k_c} = \frac{GD_c}{\sigma_n(b-a)}. \tag{3}$$

Numerical models of this nucleation process indicate that slow slip first localizes to an ~h^*-sized region—often termed the nucleation zone—where slip accelerates [e.g., *Dieterich*, 1992; *Rubin and Ampuero*, 2005; *Ampuero and Rubin*, 2008; *Fang et al.*, 2010]. The nucleation zone can expand and/or migrate in different circumstances. Laboratory experiments with large L and/or small G show a similar acceleration of slip in a localized zone, often with additional complexity [*Okubo and Dieterich*, 1984; *Ohnaka and Kuwahara*, 1990; *Kato et al.*, 1992; *Ohnaka and Shen*, 1999; *Rosakis et al.*, 2006; *Nielsen et al.*, 2010; *Ben-David et al.*, 2010; *McLaskey and Kilgore*, 2013; *Latour et al.*, 2013; *Selvadurai and Glaser*, 2017].

We note that it is not usually straightforward to translate the critical stiffness concept into a length, as is implied by equation (3), since, in general, fault stiffness can vary in space and time due to varying slip rates during nucleation of a slip instability [e.g., *Rubin and Ampuero*, 2005; *Ampuero and Rubin*, 2008; *Segall et al.*, 2010]. Alternative definitions of h^* are common. *Rubin and Ampuero* [2005] defined

$$h^*_\infty = \frac{GD_c b}{\pi\sigma_n(b-a)^2}, \tag{4}$$

and a linear slip weakening friction model produces a critical length scale of the form [*Okubo and Dieterich*, 1984]:

$$h^*_{L_c} = \frac{c_1 GD_c\left(\mu_p - \mu_r\right)}{\sigma_n(\mu_0 - \mu_r)^2}, \tag{5}$$

where c_1 is a geometrical constant, μ_r is a residual friction level, μ_p is a peak friction level, and $\mu_0 = \tau_0/\sigma_n$ where τ_0 is an initial stress level. Despite the ambiguity in h^*, all formulations are similar, and we believe that it is a useful parameter for gaining a general understanding of faulting behavior.

A parameter space that maps stability behavior is shown in Figure 1. The red dashed line shows behavior for small stiff samples ($k_{\mathrm{sample}} >> k_{\mathrm{machine}}$), while the blue line maps large compliant samples ($k_{\mathrm{sample}} << k_{\mathrm{machine}}$). Behavior is separated into stable sliding (quadrant II) and two flavors of stick-slip motion. For $L/h^* << 1$ (quadrant I) the sample behaves much like a rigid block and the sample accelerates quasi-uniformly in a stick-slip instability that is fueled by the compliance of the loading machine (slider-block-like behavior). For $L/h^* >> 1$ (quadrant III), a stick-slip instability nucleates within the sample and is fueled by the compliance of the sample itself (continuum-like behavior). Quadrant IV is inaccessible, in practice. For example, assuming that $k_{\mathrm{sample}} \approx C_0 G/L$, where C_0 is a geometrical constant, maximizing both the y axis $k/k_c \approx C_0 G L^{-1} k_c^{-1}$ and the x axis $L/h^* \approx L k_c G^{-1}$ amounts to maximizing C_0, which has physical limitations.

Episodic slow slip behavior occurs near the transition between stick-slip and steady sliding, indicated by the hashed region. For slider-block-like experiments, SSEs occur between quadrants (I) and (II), as indicated by

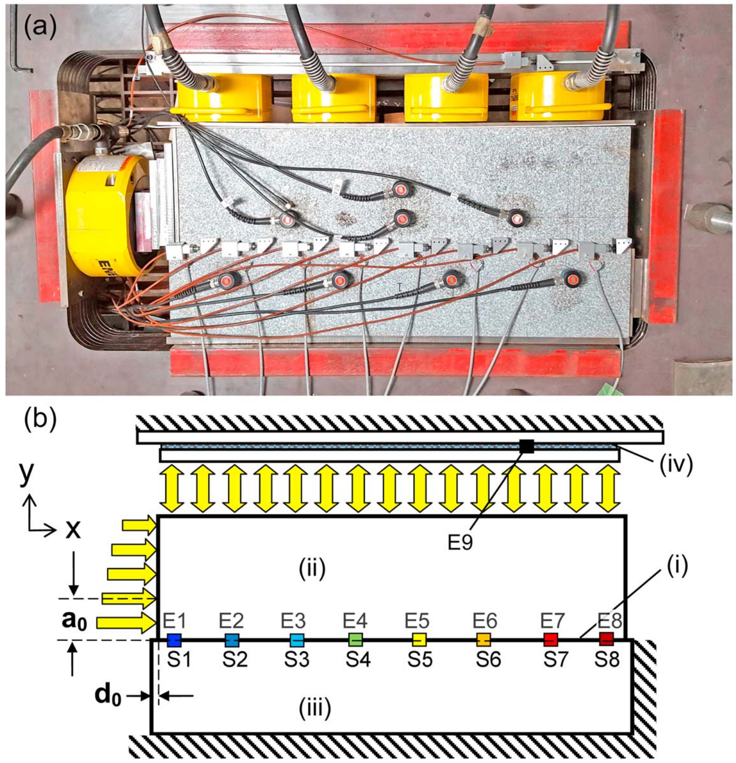

Figure 2. (a) Photograph and (b) schematic diagram of the sample and apparatus. The two granite samples are 0.76 m long and are placed in a steel loading frame. Forces are applied to the samples with five hydraulic cylinders (yellow). Slip sensors (E1–E8) and strain gage pairs are placed at eight locations along the length of the fault. Slip of the Teflon/steel low friction interface is also measured (E9). An array of piezoelectric sensors (red and black circles) detect ground motions.

the double arrow labeled "A." For example, *Leeman et al*. [2016] increased k or decreased σ_n to force a sample to transition from DSEs to SSEs to steady sliding. Other researchers also observed a transition between quadrants (I) and (II) by altering k_c either by continued wear of the fault surface [*Voisin et al*., 2007; *Gu and Wong*, 1994] or by temperature-induced changes to friction properties [*Okazaki and Katayama*, 2015]. We believe that the SSEs observed in the current study are generated between quadrants (II) and (III) described by the double arrow labeled "B" in Figure 1.

3. Overall Mechanics of the Experiment

A photograph and schematic diagram of our direct shear apparatus is shown in Figure 2. Two 760 mm long rectangular granite blocks are squeezed together and sheared past one another. Slip occurs on both a rock/rock simulated fault (i) and a Teflon/steel low friction interface (LFI) (iv). A simplified spring-slider system is shown in Figure 3 that is mechanically similar to the apparatus even though it differs geometrically. The VW block represents the rock/rock simulated fault of length L = 760 mm. The VS block represents the LFI. Each block is connected to a rigid bar such that load point displacement at c_5 increases shear stress on both the LFI and the simulated fault. Spring k_3 connects the two blocks, so that slip on the LFI causes increased shear stress on the simulated fault and vice versa.

In a typical experiment, shear load is increased by advancing the hydraulic cylinder c_5, shown in yellow on the left side of Figure 2a. The LFI ($\mu \approx 0.1$) is substantially weaker than the rock-rock fault ($\mu \approx 0.8$) and therefore begins to slip first. As a result, the fault is loaded by the hydraulic cylinder and by the slow slip of the VS LFI. Figure 4 shows a DSE ($t \approx 475$ s) and a SSE ($t \approx 520$ s) characterized by sudden drops in sample average shear stress (Figure 4a), peaks and drops in local shear stress (Figure 4b), and sudden increases in fault slip (Figure 4c). Slip on the rock/rock fault forces slip on the LFI. The LFI often hosts slow slip events of its own ($t = 442$ s, 460 s, and 485 s). These LFI slip events typically involve ~10 μm of slip and have not been observed to trigger events on the rock/rock fault.

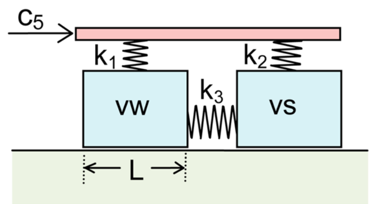

Figure 3. A simplified mechanical model of the experiment. The velocity-weakening block (VW) represents the 760 mm long rock/rock simulated fault. The velocity-strengthening (VS) block represents the Teflon/steel low friction interface. Increased hydraulic pressure in cylinder c_5 increases shear stress on both the low friction interface and the simulated fault. Slip on the LFI causes increased shear stress on the simulated fault and vice versa, as indicated by connecting spring k_3.

We roughly estimate h^* for our experiment based on G = 30 GPa, σ_n = 14 MPa, and assume $(b - a) \approx 0.004$ and $D_c \approx 1$ μm for the granite fault with little gouge. From equation (3), we find $h^* \approx 0.5$ m, which is close to the sample length L = 0.76 m. Since $h^* \approx L$, an instability will begin to nucleate, but the VW sample is not large enough to fully support nucleation up to ~m/s slip speeds. The nucleation zone expands to the sample ends and runs out of elastic strain energy that fuels the instability. Stress transferred to the VS LFI helps quench the instability, resulting in a SSE. On the other hand, if $h^* < L$ then a slip instability can nucleate within the VW fault and accelerate to seismic slip speeds before the edges of the sample are ruptured; a DSE is generated independent of the VS LFI. Our estimates of h^* likely have only order-of-magnitude accuracy due to uncertainty associated with the formulation (equation (3)), the underlying parameters D_c and $(b - a)$, and the applicability of the formulation to a sample of finite size L and associated edge effects.

Fast or slow events are generated simply by changing the loading conditions. Positive loading rate has been shown to cause instabilities or accelerations of a slider block to occur even when $k > k_c$ [*Rice and Gu*, 1983; *Gu et al.*, 1984; *Helmstetter and Shaw*, 2009]. Our experiments show a related effect, except that the sample

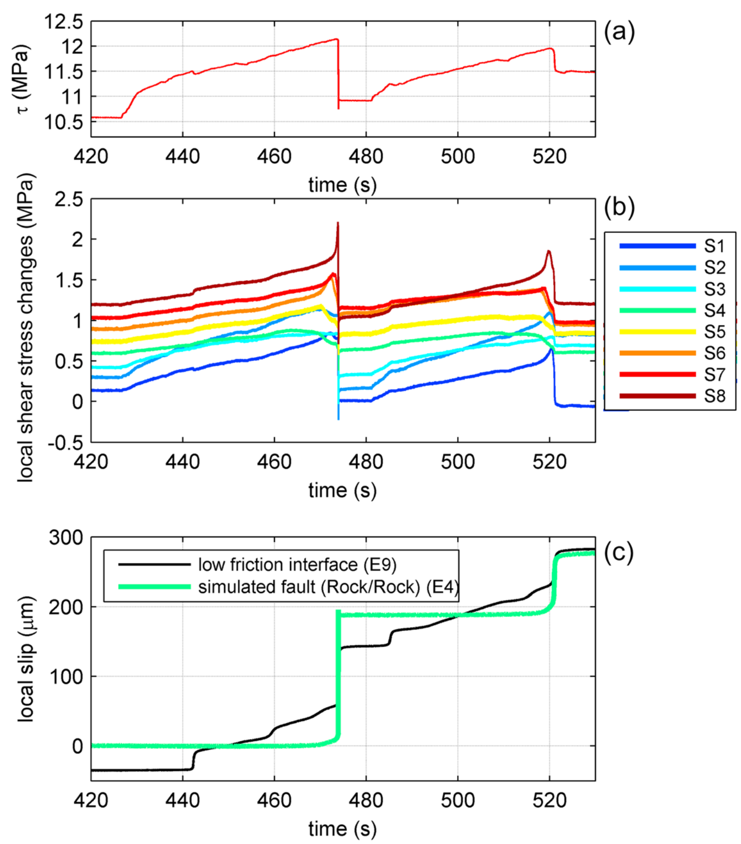

Figure 4. Two successive slip events (#2 and #3 from Figure 5) on the simulated fault and the interactions between (a) sample average shear stress derived from hydraulic pressure c_5, (b) local shear stress derived from strain measurements (S1–S8), offset for clarity, and (c) fault slip measured near the center of the simulated fault (E4) and on the low friction interface (E9). The data shown in Figure 4a are a subset of the data shown in Figure 5 (dotted box).

cannot be treated as a simple slider block, since $h^* \approx L$. Instead, we argue that loading rate, as well as healing time, can affect the spatial and temporal extents of the nucleation zone, such that an instability can nucleate on a fault patch that is either smaller or larger than the h^* expected under slow and constant loading conditions. This is consistent with some experimental observations [*Kato et al.*, 1992] and numerical models [*Kaneko and Lapusta*, 2008; *Kaneko et al.*, 2016]. Our results illustrate a complex dependence of stability on loading rate and healing time described in section 6.

4. Methods

4.1. Sample and Loading

Experiments were conducted on a direct shear biaxial apparatus that accommodates a pair of Barre gray granite blocks as shown in Figure 2. Deformation occurs on a simulated fault (i) that is the interface between a moving rock block (ii) and a longer stationary rock block (iii). The dimensions of the moving block are 762 mm × 203 mm × 102 mm in the x, y, and z directions, and dimensions of the stationary rock block are 787 mm × 152 mm × 102 mm in the x, y, and z directions. The simulated fault is 762 mm × 102 mm with area $A = 0.078$ m^2. The two blocks are pressed together in the y direction with four hydraulic cylinders c_1–c_4 that apply a constant normal stress (σ_n) on the simulated fault. Shear stress is applied to one end of the moving block with hydraulic cylinder c_5 through a steel loading platen composed of a stack of steel plates, as depicted in Figure 2a. Deformation also occurs on a LFI (iv) composed of a 2.4 mm thick sheet of reinforced Teflon sandwiched between two sheets of 13 mm thick precision ground steel. In an experiment, the moving block and cylinders c_1–c_4 translate in the $+x$ direction, while the other block and the remainder of the apparatus are stationary. Using a double direct shear configuration (not shown), we verified that the coefficient of friction μ of the low friction interface is between 0.10 and 0.14 and exhibits VS behavior, consistent with previous reports of Teflon sliding on steel [*Dieterich and Kilgore*, 1994; *Mokha et al.*, 1990]. The center of action of cylinder c_5 was a distance a_0 of either 38 or 50 mm from the simulated fault. This and the different friction coefficient between the LFI ($\mu \approx 0.1$) and the rock/rock simulated fault ($\mu \approx 0.8$) introduces a net moment to the moving rock block and can contribute to a nonuniform distribution of normal stress along the simulated fault.

The surfaces of the blocks were prepared by the manufacturer to be flat and parallel to 125 μm. Experiments were performed after a "run in" period whereby the two blocks were forced to slide past each other under normal load (3–14 MPa) for tens of millimeters of cumulative slip. The two rocks were separated occasionally to inspect the fault surface. A small amount of fine rock flour (gouge) was produced as a result of sliding (estimated to be a few tens of micrometers thick) that was distributed throughout the nominal area of contact, though more wear material was observed near the ends of the samples than in the center. Striations about 20 mm long in the x direction were also observed over most of the fault surface. Gouge was not removed between experiments or before the start of the experiments.

At the beginning of each experiment, the moving block was reset to a specified offset d_0 relative to the edge of the stationary block. Normal stress σ_n was held constant at a specified value between 2 and 20 MPa. This was accomplished simply by closing a valve such that the volume of hydraulic fluid remained constant in cylinders c_1–c_4. Shear stress τ was then increased at a relatively constant rate $\dot{\tau} \approx 0.02$ MPa/s by increasing the hydraulic pressure in cylinder c_5 until a slip event occurred. (It should be noted that in this approach, σ_n is not entirely constant but is coupled to τ through the Poisson effect which produces a 140 kPa increase in σ_n for 1 MPa increase in τ.) Slip events consisted of tens to hundreds of microns of slip on the simulated fault and a measurable drop in sample average shear stress. An example sequence of slip events are numbered in Figure 5. After a slip event, τ was held constant for a set period of time t_{hold} after which the sample was reloaded to produce another slip event. Loading rates were varied between 0.01 MPa/s and 2 MPa/s, and hold time was varied between 0 and 500 s to study their effects. By varying only these two parameters, we were able to generate sequences of events that switched back and forth between SSEs and DSEs. Sample average shear and normal stress were calculated from hydraulic pressure measured in c_5 and c_1–c_4, respectively.

4.2. Slip Measurements

Eddy current displacement sensors were used to measure local fault slip along the top trace of the simulated fault at eight locations (E1–E8) shown in Figure 2b and one location on the LFI (E9). These measure

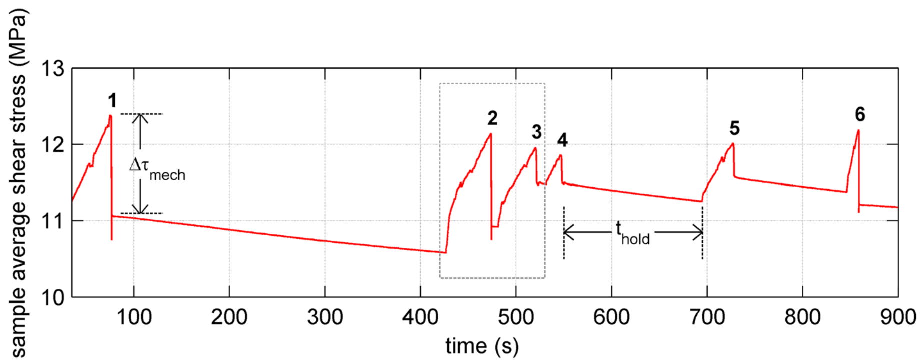

Figure 5. An example of loading data from one of 21 experimental runs. This example shows a sequence of six slip events generated at σ_n = 14 MPa. The first two events are DSEs with peak slip velocities of 180 and 150 mm/s, respectively, and sample average shear stress change $\Delta\tau_{mech}$ of more than 1 MPa. Events #3 and #4 are SSEs with peak slip velocities of 410 and 360 μm/s, respectively, and smaller $\Delta\tau_{mech}$. Events #5 and #6 have peak slip velocities of 47 and 110 mm/s. These events slip faster and are more unstable than the two previous events due to increased hold time t_{hold} (event #5) and increased loading rate (event #6).

displacement between a probe housed in an aluminum holder glued onto the stationary rock block and a target glued to the moving rock block, as shown in Figure 6. Fault slip caused the target to translate away from the probe. The sensors are stable at low frequencies (>1 h periods) and have a flat sensitivity up to 10 kHz. Data were recorded at 50 kHz and then averaged to 5 kHz to reduce high-frequency noise. A mechanical resonance of the probe and target can cause distortions when subjected to rapid accelerations (~ 500 m s^{-2}). This is the cause of the overshoot and damped oscillation (~400 Hz frequency that persists for 5 to 10 ms) visible in many of the figures.

4.3. Strain Measurements

Local shear strain γ was measured at eight locations (S1–S8) that are essentially collocated with the slip measurements E1–E8, as shown in Figure 6. At each location, a pair of collocated strain gages with 5 mm gage length, oriented at 45° and 135° from the fault, were glued to the stationary block 14 mm from the fault. Local shear strain γ was derived from the differences of the strain in the two gages, and we assume a shear modulus of $G = 30$ GPa to derive local shear stress $\tau = G\gamma$. Figure 4b shows strain measurements S1–S8 for two successive slip events.

4.4. Ground Motion Measurements

An array of 11 piezoelectric sensors (Panametrics V103, 13 mm diameter) were glued directly to the granite sample on both the top and bottom surfaces. These sensors are sensitive to vertical ground motions, and their output (voltage) is roughly proportional to surface-normal displacement (20 mV/nm) in the 100–300 kHz frequency band that dominates these recordings [*McLaskey et al.*, 2014]. We quantified the magnitude of seismic events in the frequency domain using an empirical Green's function technique that utilizes a ball impact as an absolute reference source, as described in section 5.4. Details of the various sensors are summarized in Table 1.

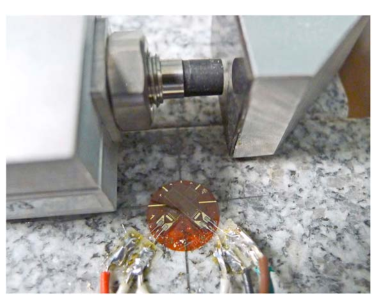

Figure 6. A photograph of a strain gage pair glued to the stationary block 14 mm from the fault and an approximately collocated eddy current sensor that measures local fault slip. The eddy current sensor measures displacement between a probe (black cylindrical piece), attached to the stationary rock block, and a target, attached to the moving rock block.

5. Results

We conducted 21 experimental runs similar to the one described above and varied applied σ_n between 2 and 20 MPa, a_0 between 38 and 50 mm, and d_0 between 0 and 17 mm (see section 4.1). We characterized three parameters for each slip event in each experiment: sample average fault slip

Table 1. Summary of the Sensors Utilized in the Experiments

Physical Quantity	Sensor Type	Notation	Bandwidth	Sampling Rate (kHz)	Recording Mode
Local fault slip	eddy current	E1–E9	~1 mHz to 10 kHz	50, averaged to 5	continuous
Local shear strain	strain gage pair	S1–S8	~1 mHz to 10 kHz	5	continuous
Vertical ground motion	piezoelectic	PZ1–PZ11	100 Hz to 1 MHz	5000	triggered
Sample average normal and shear stress	hydraulic pressure	c_1–c_4, c_5	~1 mHz to 1 kHz	5	continuous

d, sample average maximum slip rate $\dot{d}_{max}$, and the sample average shear stress change $\Delta\tau_{mech}$ derived from changes in hydraulic pressure in cylinder c_5. We defined d as the slip that occurred within a 2 s time window centered on the time of the peak slip rate, shown in Figures 7a and 7b insets. The 2 s time window adds to d premonitory slip or afterslip but ensures that d is not affected by overshoot and oscillation associated with mechanical resonance of the eddy current sensor holders. For both d and $\dot{d}_{max}$, we take the average of the measurements from the eight slip sensors (E1–E8).

5.1. Stiffness Calculation

Figure 8 shows sample average fault slip d plotted against shear stress change $\Delta\tau_{mech}$. Each symbol is a slip event from one of 11 different experimental runs. The largest events were generated at the highest σ_n ($\Delta\tau_{mech}$ = 4 MPa, d = 600 μm of slip at σ_n = 20 MPa). All events follow the same linear relationship between d and $\Delta\tau_{mech}$ that is used to estimate the loading system stiffness k = 6 GPa/m (equation (2)).

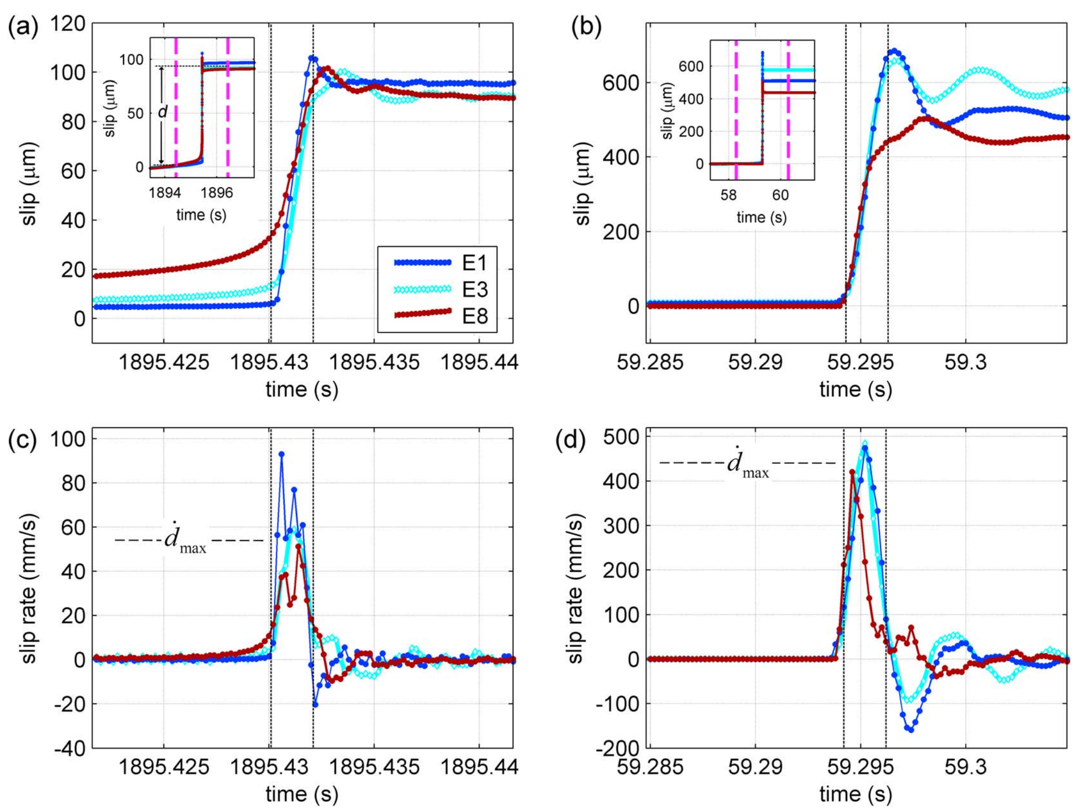

Figure 7. Eddy current slip sensor data showing local fault slip measured at three locations along the simulated fault for DSEs generated at (a) σ_n 7 MPa and (b) σ_n 20 MPa. Slip in Figures 7a and 7b are shown relative to the slip 1 s prior to the slip event. (c and d) Local slip rate is derived from the first difference of the slip data. We parameterize slip events by $\dot{d}_{max}$ the average of the peak slip rate determined from the eight slip sensors located along the length of the simulated fault (E1–E8) and the slip d which we define as the slip that occurred within a 2 s time window centered on the time of the peak slip rate (magenta dashed line in the insets). The vertical black dotted lines show 2 ms time windows that correspond to the duration of rapid sliding T, which is essentially constant for all DSEs generated and is independent of moderate variations in d.

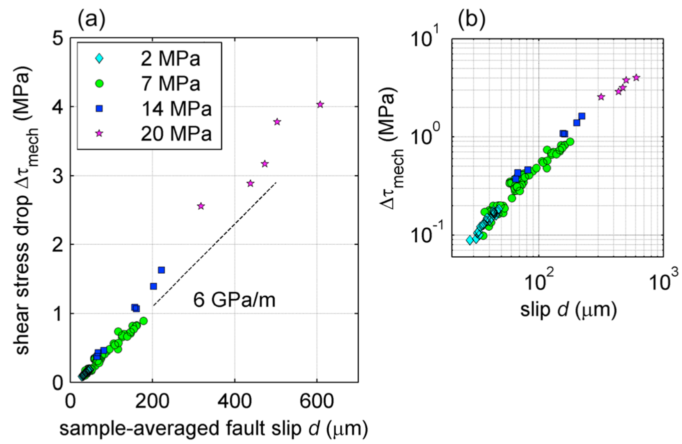

Figure 8. (a) Sample average fault slip d and sample average shear stress change $\Delta\tau_{\mathrm{mech}}$. Each symbol corresponds to a different slip event from one of 11 different experimental runs. (b) The same data are plotted on a log-log scale. The slope of the linear relationship indicates the loading system stiffness $k = 6$ GPa/m. Some of the observed scatter is likely due to changing d_0 from 0 to 17 mm which causes a slight increase in k. Other scatter could be due to the differing slip rates on the LFI during the slip events which would affect the measurement of $\Delta\tau_{\mathrm{mech}}$ but not d.

5.2. Constant *T* and Comparison Between Large and Small DSEs

DSEs of different magnitudes are of the same duration T. This scaling behavior differs from earthquakes where larger events are longer. We find that T is approximately constant for all DSEs generated on this machine and is independent of moderate changes in σ_n (7–20 MPa) and d (~100 to 600 μm). Figure 7 compares a small DSE generated at $\sigma_n = 7$ MPa to a large one at $\sigma_n = 20$ MPa. Figures 7c and 7d show slip rate determined from the first difference of the slip sensor output. The duration of rapid sliding T is about 2 ms for both events, as indicated by the vertical black dotted lines. The factor of 5 increase in total slip d for the DSE at $\sigma_n = 20$ is entirely the result of an increase in slip rate rather than an increase in T.

Constant T has been reported on other biaxial machines [*Johnson and Scholz*, 1976] including the USGS 2 m machine [*Okubo and Dieterich*, 1984; *McLaskey and Kilgore*, 2013], and the NIED shaking table machine [*Togo et al.*, 2015]. T is constant despite twentyfold variation in d [*McLaskey et al.*, 2012]. *Kilgore et al.* [2017] systematically varied k on a single apparatus and found $T \approx$ constant for stick-slip events generated at a given k and a relationship between k and T that was somewhat different from the $kT \approx$ constant *McGarr* [2012] hypothesis.

5.3. A Break in Scaling Between DSEs and SSEs

Figure 9 shows $\dot{d}_{\max}$ plotted against d. Here the events separate into two trends: audible DSEs and extended duration SSEs ($\dot{d}_{\max} < 30$ mm/s) that are faintly audible or completely silent. The DSEs fall on a line that has a slope of 1 in log-log space indicating a linear relationship between d and $\dot{d}_{\max}$ of the form

$$d = \eta T \dot{d}_{\max}, \tag{6}$$

where T is the duration of rapid sliding, and η is a shape parameter that describes the shape of the $\dot{d}$-versus-time curve. For a boxcar $\eta = 1$ (constant sliding velocity), $\eta = 0.5$ for a triangle, and $\eta = 0.6366$ for a half sine. The linear relationship indicates that ηT is approximately constant for DSEs. We find that a shape parameter $\eta = 0.6$ provides a reasonable fit to the DSE data and causes T derived from equation (6) to match $T = 2$ ms estimated directly from slip-versus-time signals. For SSEs, the $\eta = 0.6$ assumption yields T estimates that are accurate to a factor of 2 (i.e., η easily falls in the 0.4 to 0.8 range). We prefer to estimate T from equation (6) because (1) the mechanical oscillations of the slip sensor can make automated determination of T challenging for the DSEs and (2) for SSEs, T is not well defined from direct measurements of slip, as shown in Figure 10b. Figure 9b shows that DSEs have approximately constant T with varying moment, and SSEs have approximately constant moment with varying T.

5.4. Details of Slip and Seismicity

In the next sections, we focus on events #2 and #3 shown in Figure 4. These are a representative DSE ($\dot{d}_{\max}$ = 150 mm/s) and SSE ($\dot{d}_{\max}$ = 410 μm/s) both generated at $\sigma_n = 14$ MPa. Figure 10 shows details of their slip and

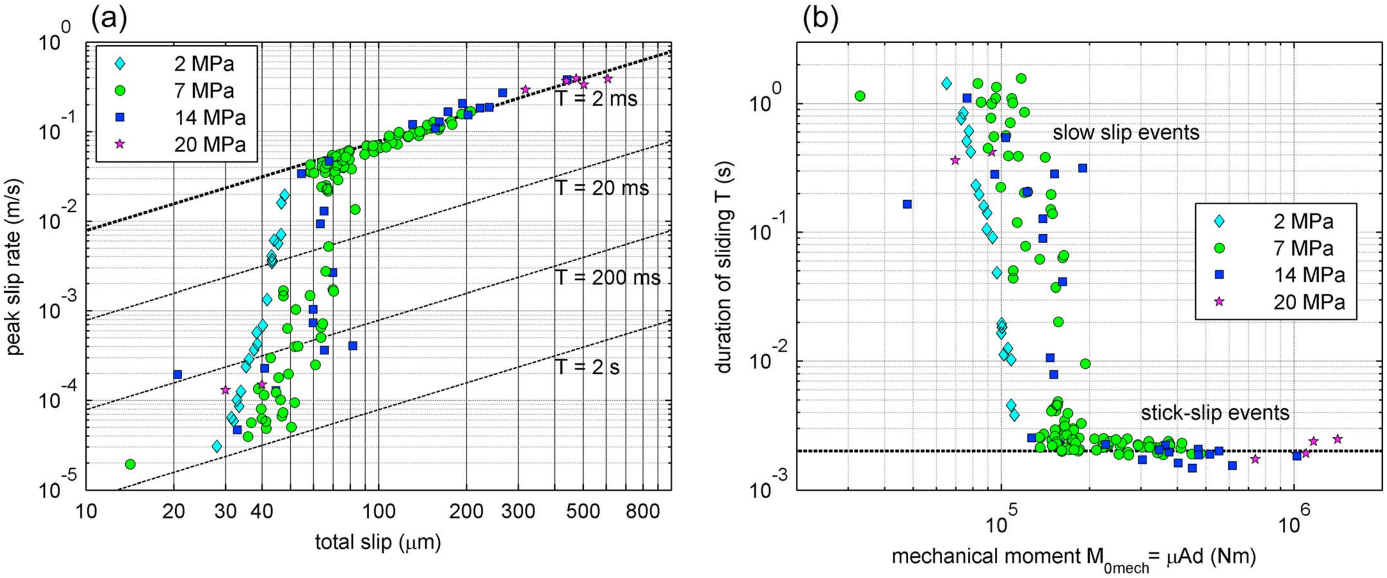

Figure 9. (a) Peak slip rate $\dot{d}_{max}$ plotted against sample average fault slip d. Each symbol corresponds to a different slip event. Events with higher slip and slip rate fall on a line with a slope of 1 which indicates a constant slip duration $T = 2$ ms, consistent with previous observations of fast "stick-slip" events. Events with lower slip and slip rate fall below this line indicating longer slip duration. Lines of constant slip duration are shown for reference. (b) The same data plotted in Figure 9a are converted to a moment duration plot by assuming $M_0 = GAd$ and $T = \frac{d}{\eta \dot{d}_{max}}$; see equation (6).

seismicity on identical time and amplitude scales for direct comparison. During the DSE, the rock/rock fault (E1–E8) slips about 170 ± 10 μm with only about 1 μm of afterslip. T is about 2 ms (vertical dashed lines in Figure 10e), consistent with section 5.2. The SSE slips ~50 μm for ~150 ms, but the beginning and end of the SSE are harder to pinpoint.

The DSE is preceded by a few M −8 to M −6 foreshocks that increase in magnitude and culminate with the DSE. A few aftershocks are also generated. Ground motions are shown in Figures 10c and 10d (100–500 kHz bandpass filter) and Figures 10g and 10h (300–500 kHz bandpass filter). These are signals recorded from a line of seven piezoelectric sensors (PZ1–PZ7) glued 50 mm from the fault at evenly spaced distances. The main seismic release of the DSE is about 2 ms in duration. The magnitude of the events is determined from the low-frequency level of the seismic source spectrum, as described in section 5.6. The foreshocks range from M −6 (at t = 473.945 s) and M −6.5 (t = 473.929 s) down to about M −8. The SSE produced swarm-like seismicity with the largest of the approximately hundreds of detectable $M \geq -8$ events near the time of peak slip rate (M − 6 and t = 521.062 s, Figure 10h).

5.5. Slow Precursory Slip and Afterslip

Figure 11 shows premonitory creep and afterslip for 20 s time windows surrounding a DSE and a SSE. The plots utilize a multi-filter algorithm described in the supporting information. Ten seconds before the DSE (Figure 11a), slip rate on the low friction interface (E9) is relatively constant and close to the externally applied loading rate of 2–5 μm/s = $\dot{\tau}/k$, where shear stressing rate $\dot{\tau}$ = 0.02 MPa/s and loading system stiffness k = 6 GPa/m. The leading edge of the moving rock (E8) is effectively locked, while the other sections of the fault slip at ~100 nm/s. In about 7 s, slip accelerates and culminates in a DSE ($\dot{d}_{max}$ = 180 mm/s). This forces a sudden increase in the slip rate on the low friction interface (E9). Approximately 1 μm of afterslip was observed on the simulated fault. Larger afterslip rates were observed on sections with smaller local stress drop. Afterslip velocity is moderately well modeled by $V = V_0/(1 + t/t^*)^p$ with $p \approx 1$ [*Helmstetter and Shaw*, 2009]. Here t^* refers to a reference time and V_0 is a reference velocity. The low friction interface decelerates more slowly, with higher afterslip rates and p value closer to 1.75. For the SSE ($\dot{d}_{max}$ = 410 μm/s, Figure 11b), slip rates are more uniform on both the simulated fault (E1–E8) and the low friction interface (E9). Afterslip is uniform with a p value ≈ 1.25.

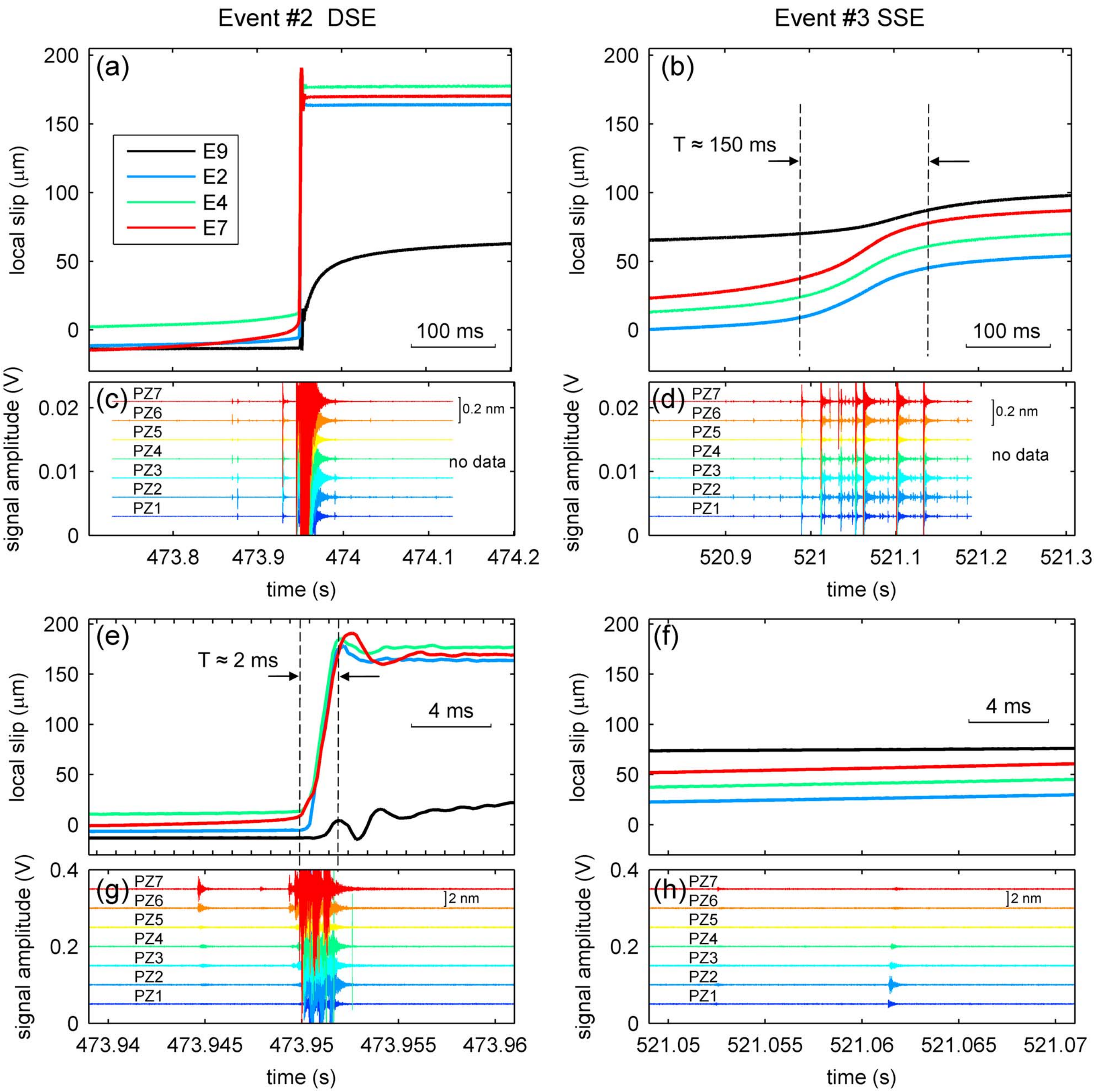

Figure 10. Direct comparison of slip and seismicity of fast and slow events (#2 and #3 from Figure 5) generated at σ_n = 14 MPa. (a, b) Local slip measured at three locations on the simulated fault (E2, E4, and E7) and on the low friction interface (E9). (c, d) Ground displacement recorded from seven piezoelectric sensors shows that the fast DSE produced a large seismic event with a few foreshocks and aftershocks, while the SSE produced a swarm of small events. (e, f) A zoom in of the 22 ms surrounding the slip events shows that the duration of sliding is about 2 ms for the DSE. (g, h) Seismicity in the same time window as Figures 10e and 10f shows a comparison between the largest event in the SSE-generated swarm and the largest ground motions produced by the DSE. Slip accumulated during the SSE is about a third to a half of the amount accumulated in the DSE, but because peak slip velocity is about 500 times lower than the DSE, the SSE has 500 times smaller seismic coupling.

5.6. Source Spectra, Seismic Moment, and Seismic Coupling

The source spectra of DSEs, SSEs, foreshocks, and aftershocks are determined by comparing the spectra of recorded ground motions to the spectra of ground motions from a reference source. The reference source is either a smaller seismic event or the impact of a tiny ball on the top surface of the rock sample. The technique is essentially the same as an empirical Green's function technique [e.g., *Frankel and Kanamori*, 1983; *Mueller*, 1985; *Hutchings and Wu*, 1990; *Hough and Dreger*, 1995] except that the ball drop reference source

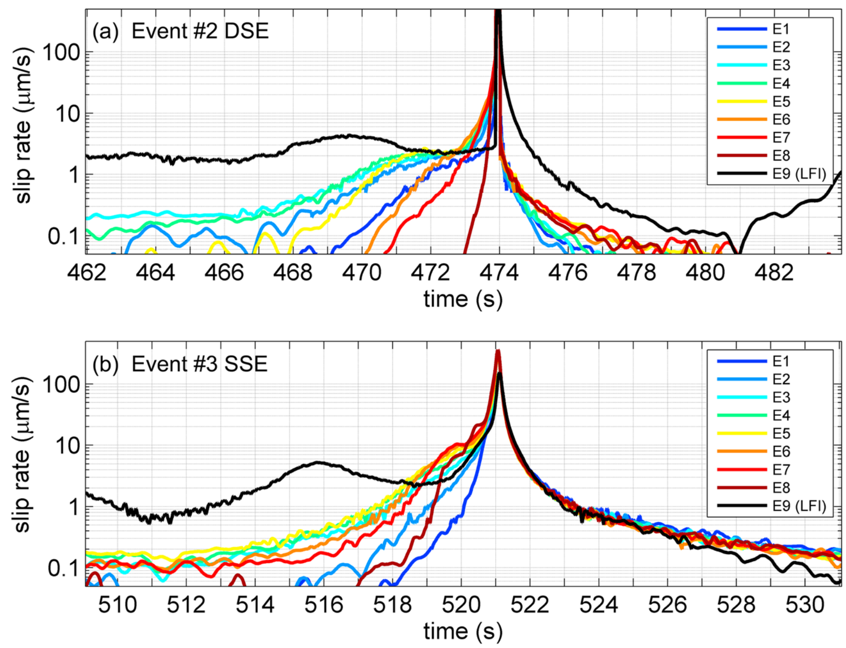

Figure 11. Details of the rate of premonitory slip and afterslip in the 22 s surrounding (a) a DSE and (b) a SSE recorded at eight locations along the simulated fault (E1–E8) and at one location on the low friction interface (E9). Afterslip following the SSEs occurs coherently at all measured locations, while afterslip rates following the DSEs differ along the simulated fault. Slip rates are also more uniform along the simulated fault prior to the SSE, whereas prior to a DSE, slip rates are more heterogeneous and one end of the fault remains essentially locked until 1 s before the DSE.

amplitude is related to the change in momentum of the ball, which can be independently and absolutely determined. Further details of this technique are described in *McLaskey et al*. [2015].

Figure 12a shows the spectra of radiated waves from a DSE (filled circles), SSE (open circles), and three foreshocks of the DSE of various sizes. (These are the same slip events as those shown in Figures 4, 10, and 11). Spectra are determined from the amplitude of the Fourier transform of a piezoelectric sensor's signal tapered with a Blackman Harris window centered on the first wave arrival. We varied window lengths from 3 to 200 ms and report only spectral estimates that are stable with respect to window length. The spectra shown in Figure 12 are the average of spectra obtained from five different piezoelectric sensors. This averaging produces a more stable estimate of the amplitude spectrum that is less dependent on source-to-sensor path length or the sensor's position with respect to the radiation pattern of the source. Figure 12b shows estimates of the displacement source spectra of these events, with instrument and wave propagation effects removed. Spectra are only shown in frequency bands where both the seismic events and the reference events have adequate signal-to-noise ratio.

The source spectra of seismic events are flat at low frequencies and falloff above the corner frequency $f_c \approx 1/T$. Seismic moment is obtained from the spectral amplitude at low frequencies.

The source spectra of the M −6 to M −7.5 foreshocks are shown as triangles, squares, and diamonds in Figure 12b. We expect these small events to have f_c in the hundreds of kilohertz range based on standard earthquake scaling relationships [e.g., *Walter et al*., 2006], and the spectra shown have roughly constant amplitude since the frequency band is below f_c. For the DSE, we expect $f_c \approx 500$ Hz (since $T = 2$ ms), which is at the lower end of our resolvable frequency band. Our magnitude estimate, M −3, is thus a lower bound. The DSE has an approximately ω^{-2} high-frequency falloff, consistent with standard earthquake source models [e.g., *Aki*, 1967; *Brune*, 1970] and previous estimates of source spectra of stick-slip events generated on biaxial and triaxial machines [*McLaskey and Lockner*, 2014; *McLaskey et al*., 2015]. For the SSE, the long source duration (> 100 ms) places the corner frequency below 10 Hz, yet the source spectrum of the SSE is relatively flat in our resolvable frequency band and is nearly identical to that of the single largest event in the swarm of micro events generated by the SSE (M −6).

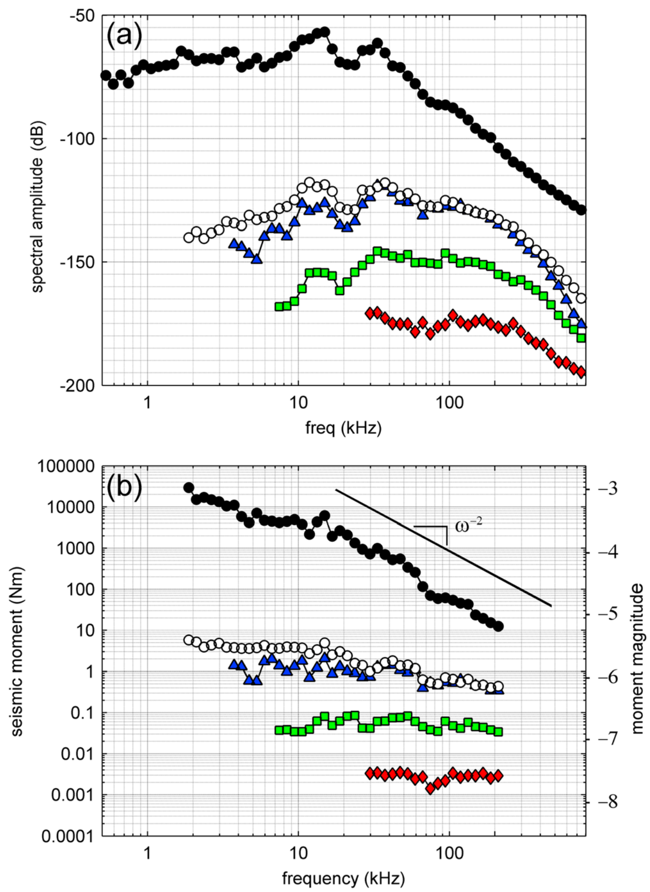

Figure 12. (a) Uncorrected spectra and (b) displacement source spectra of waves radiated from a stick-slip event (filled circles), a slow slip event (open circles), and foreshocks of various sizes that precede the stick-slip event. The blue triangles signify the largest foreshock (M −6) which occurs about 5 ms before the initiation of the stick-slip event (DSE). The green squares signify the second largest foreshock (M −6.5) that occurs 21 ms prior to the DSE. The red diamonds signify a M −7.5 foreshock that occurs 80 ms prior to the initiation of the DSE. Smaller events are detected but with insufficient SNR to perform robust spectral analysis.

To roughly estimate differences in seismic coupling between the DSE and SSE, we add up the moment of all the seismic events produced during the SSE and compare this number (5 Nm) to the seismic moment of the DSE (>10,000 Nm). Taking into account the different amounts of slip generated by the two events, we estimate that the DSE has at least 600 times greater seismic coupling than the SSE (see Table 2). In general, we find a linear relationship between seismic moment and measured slip for DSEs (total slip >80 μm and $\dot{d}_{max} > 70$ mm/s), indicating a roughly constant seismic coupling coefficient for these fast events, as shown in supporting information Figure S1. SSEs have longer source durations and therefore lower corner frequencies and significantly lower amplitude radiated waves in the frequency band we consider (~500 Hz to 500 kHz). Slower SSEs produced even weaker seismic signals, and many did not trigger our high-speed recording system.

6. Discussion

6.1. Single Direct Shear Versus Double Direct Shear Configuration

To test the effects of the VS LFI on the stability behavior of the rock/rock simulated fault, we conducted additional experiments using a double direct shear configuration with a moving rock block sandwiched between two stationary rock blocks, as shown in supporting information Figures S2 and S3. In this case, the VS Teflon LFI was substituted for a second rock-rock interface. We measured fault slip near the center of each of the two rock/rock interfaces. After a similar run in period (~30 mm of slip at σ_n = 8 MPa), we conducted experiments at σ_n = 7 MPa.

Compared to the single direct configuration with the VS LFI, a much more exact loading procedure was required to produce SSEs. This procedure involved rapid reloading after a DSE and then a decreased loading rate as the critical shear stress level was approached (see section 6.3). One of the two rock/rock faults would often begin to slip slowly, and this would trigger instability on the other rock/rock fault. This interaction complicated the nucleation process and promoted DSEs as if the effective length of the sample was longer than the length L of one of the two rock/rock interfaces. DSEs had T = 1.5 to 2 ms.

Based on the above results, we conclude that the VS LFI is not required for the generation of SSEs, but it did simplify the loading conditions felt by the rock/rock simulated fault and seemed to expand the area of parameter space over which SSEs could be generated, at least compared to the double direct shear case. The sudden increase in slip rate on the VS LFI in response to a slip event on the rock/rock simulated fault would also reload the rock/rock fault during the postseismic phase (see section 6.3) which likely promoted

10.1002/2016JB013681

Table 2. Comparison of Features of Fast and Slow Slip Events Described in Figures 4, 10, and 11

	DSE (Dynamic Slip Event)	SSE (Slow Slip Event)
Total slip, d	170 μm	50 μm
Duration of sliding, T	2 ms	~ 150 ms
Peak slip rate, $\dot{d}_{\max}$	0.18 m/s	400 μm/s
Afterslip	~1 μm	>20 μm
Max M event generated	M −3.5	M −6
Total seismic moment $M_{0\mathrm{seis}}$	~10,000 Nm	5 Nm
Mechanical moment $M_{0\mathrm{mech}}$ = G$A$$d$	400,000 Nm	120,000 Nm
Seismic coupling $C_x M_{0\mathrm{seis}}/M_{0\mathrm{mech}}$ where C_x is a constant used to relate k from a laboratory experiment to G of a fault's host rock	$0.025C_x$	$0.00004C_x$

afterslip and SSEs. A spectrum of fast and slow events could be generated without the need for finely tuned loading procedures. This generally agrees with the modeling results of *Skarbek et al.* [2012].

6.2. Nucleation and the Nonuniform Distribution of Stress

Normal stress was not uniformly distributed along the length of our sample due to the finite sample geometry and compliance of the steel load frame. While not directly measured, we estimated the normal stress distribution from finite element models of the rock samples and steel load frame. The models were also compared to measurements of the shear strain distribution (Figure 4b). Those results indicate that σ_n is relatively uniform throughout the center of the sample but increases by about a factor of 3 near the sample ends, consistent with modeling results for similar geometry [e.g., *Kammer et al.*, 2015]. When we opened the fault and inspected the surface, we observed an increased amount of striations and gouge within ~25 mm of the sample ends, indicating higher wear rates there. Other work on direct shear machines has shown a similar nonuniform distribution in normal stress [*Ben-David et al.*, 2010] and in density of asperity contacts [*Fukuyama et al.*, 2014; *Selvadurai and Glaser*, 2015].

In our experiments, slip initiates near the center of the simulated fault (Figure 11) where σ_n is lowest. This premonitory slow slip causes a reorganization of stress and results in decreased stressing rate on slipping regions and increased stressing rate felt by adjacent regions, as shown in Figure 4b and previous studies [e.g., *Ohnaka and Kuwahara*, 1990; *Kato et al.*, 1992; *Ohnaka and Shen*, 1999; *McLaskey and Kilgore*, 2013]. With continued loading, the slipping region expands and slip and stress changes accelerate. Eventually, this nucleation culminates in a slip event that produces slip on the entire simulated fault. The nonuniform σ_n as well as the finite sample size and associated edge effects likely affect the nucleation properties and h^* observed.

6.3. Dependence of Stability on Loading Rate and Healing Time

Previous studies of the effects of loading parameters on either the stability of slider blocks or the nucleation properties of continuum like cases revealed a complex relationship between loading rate and stability, likely because healing time is another important factor, and these two effects cannot be fully separated [*Kato et al.*, 1992]. Some studies show that increased loading rate promotes stability: higher loading rate decreases the amplitude of stick-slip instabilities [e.g., *Karner and Marone*, 2000] or promotes stable sliding [e.g., *Baumberger et al.*, 1994; *Gu and Wong*, 1994]. These experiments were conducted with external loading rate held constant throughout many cycles of slip instabilities. On the other hand, *sudden increases* in loading rate promote instability. Increased loading rate associated with velocity step tests or after the hold period of slide-hold-slide experiments can produce accelerations akin to slow slip events or DSEs in extreme cases. *Gu et al.* [1984] studied rate- and state-dependent friction equations applied to a slider block initially sliding stably (i.e., at steady state) and found that increased loading rate can induce unstable slip even when $k > k_c$. A similar instability occurs if loading is paused, allowing the fault to heal, and then resumed at the same rate. Increased loading rate and the resumption of loading after a hold both drive the system above steady state, and we will refer to this as a "kick" to the fault system.

Our experiments indicate that stability behavior depends strongly on when in the loading cycle a kick is applied. Rather than sliding at steady state, the natural earthquake cycle under slow tectonic loading likely oscillates about steady state in what are sometimes called interseismic, nucleation, coseismic, and

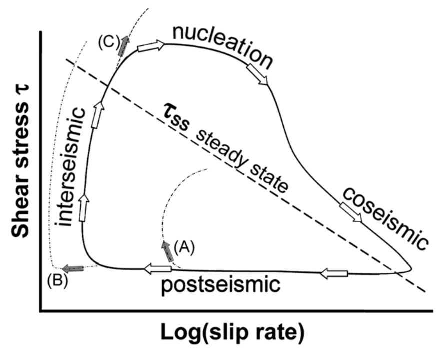

Figure 13. A diagram of the earthquake cylce for a VW fault patch that includes nucleation, coseismic, postseismic, and interseismic phases. Increased loading velocity applied during the postsiesmic phase (before the fault has adequately healed) can push the cycle toward steady state (A) and stifle instability. Longer healing times (B) and increases in loading rate later in the cylce (C) push the cylce far above steady state and promote instability. Adapted from *Fang et al.* [2010].

postseismic phases, as depicted in Figure 13 [*Fang et al.*, 2010]. Periodic slip events generated in a laboratory undergo a similar cycle (stick-slip cycle).

If loading rate is increased immediately following a DSE (in the postseismic phase), it will kick the system toward steady state and will promote stability. This is shown as alternate path (A) in Figure 13. In our experiments, SSEs are most easily generated by rapidly reloading the sample immediately following the previous slip event and then reducing the loading rate as the critical stress level is approached. This scenario encourages coherent afterslip, minimizes fault healing, and also minimizes the rate of loading felt by the fault during nucleation of the next slip event. On the other hand, a long hold period (alternate path B) or increased loading rate near the end of a stick-slip cycle (alternate path C) will kick the system far above steady state and will promote large-amplitude DSEs. In our experiments, DSEs are most easily generated with long hold times followed by rapid loading rate.

6.4. Dependence of h^* on Loading Rate and Healing Time

For larger samples ($h^* \approx L$ or $h^* < L$), we believe that an increased propensity for instability described above can be interpreted as causing the size of the nucleation zone to shrink relative to the h^* expected under slower loading conditions. We do not suggest that D_c or $b - a$ in equation (1) depend on loading velocity; variations are likely caused by additional factors that are not considered in the formulation of h^* (equation (3)). This interpretation is supported by experiments on a 50 mm granite fault that showed that slower loading produced more stable slip events and larger h^* while faster loading promoted instability and reduced h^* [*Kato et al.*, 1992]. The loading rate was imposed after a hold period $t_{\text{hold}} = 20$ min. Experiments on a 2 m granite fault showed that reduced h^* and larger-amplitude instabilities resulted from longer t_{hold} at the same loading rate [*McLaskey and Kilgore*, 2013]. Numerical models employing rate- and state-dependent friction showed that a small but abrupt increase in shear stress late in the earthquake cycle can reduce h^* by an order of magnitude [*Kaneko and Lapusta*, 2008]. When load is applied gradually (<1 MPa/h) throughout the entire earthquake cycle, h^* showed little dependence on a loading rate [*Kaneko et al.*, 2016].

We also find that the larger amount of afterslip following a SSE (Figure 11) encourages the generation of another SSE. As a result, SSEs are often produced in succession. A long hold or a sudden increase in loading rate is required to switch the faulting mode back to DSE.

6.5. Dependence on Normal Stress

Both h^* and k_c are theoretically dependent on normal stress σ_n [e.g., *Dieterich*, 1992]. Higher σ_n decreases k/k_c and increases L/h^* and has been shown to promote stick-slip events [e.g., *Scholz et al.*, 1972; *Dieterich*, 1978]. *Latour et al.* [2013] described experiments that support this theory: inverse relationship between h^* and σ_n. Our results do not provide direct evidence for decreased h^* with increasing σ_n but are generally consistent with this interpretation. Only SSEs could be generated at low normal stress ($\sigma_n = 2$ MPa), suggesting that h^* ($\approx$ 3.8 m estimated from equation (3)) was somewhat larger than L (0.76 m). Both SSEs and fully dynamic DSEs occurred at higher normal stress (($\sigma_n = 7$ MPa, $h^* \approx 1.1$ m) and ($\sigma_n = 14$ MPa, $h^* \approx 0.5$ m)). It was more difficult to achieve slow slip at $\sigma_n = 20$ MPa ($h^* \approx 0.4$ m).

6.6. Scaling Behavior Affected by LFI

The scaling of $\dot{d}_{\max}$ and d shown in Figure 9a indicates that the laboratory-generated SSEs exhibit somewhat regular behavior over a range of $\dot{d}_{\max}$ from 30 μm/s to 10 mm/s. This moment duration scaling behavior could be affected by the specific characteristics of the VS LFI and should not be interpreted as indicative of scaling behavior of naturally occurring slow earthquakes. On the other hand, slip events with peak slip rates exceeding 70 mm/s are so rapid that slip on the simulated fault has essentially stopped before the LFI has slipped more than a few microns (see Figure 10e). The scaling of DSEs with $\dot{d}_{max}$ larger than 70 mm/s is consistent with other slip events produced on other apparatuses that use either roller bearings or a different loading configuration [e.g., *Kilgore et al.*, 2017; *Johnson and Scholz*, 1976; *Togo et al.*, 2015], so we conclude that they are unaffected by specifics of the LFI.

6.7. Differences in Seismicity Between Fast and Slow Slip

The break in scaling at 30–70 mm/s (Figure 9) corresponds to a difference in the form of seismicity produced from the slip events. DSEs produced a single episode of large-amplitude shaking equivalent to a $M\ -3$ earthquake surrounded by only a few discrete foreshocks and aftershocks. SSEs produced swarms of tiny seismic events. For both DSEs and SSEs, the tiny seismic events ($\leq M\ -6$) are dynamic rupture of a small portion of the fault, at most millimeters in size, and are likely related to wear of the sample surfaces. Fast DSEs showed seismic coupling that was approximately constant, but slip events became increasingly aseismic at lower slip rates. SSEs are mostly aseismic; they often produced less than 1% of the seismic moment of DSEs (Table 2).

6.8. Implications for Tectonic Tremor and Repeating Earthquake Sequences

Our results may be applicable wherever faults exhibit transitional behavior (both creep and produce small earthquakes) or are not fully coupled. Such areas likely contain both VS and VW fault sections. Potentially seismogenic VW sections see highly variable loading rates since they are affected not just by tectonic loading but by slow slip of neighboring fault sections [e.g., *Lui and Lapusta*, 2016]. Heterogeneous VS-VW models have been used to explain repeating earthquake sequences [e.g., *Vidale et al.*, 1994; *Marone et al.*, 1995; *Chen and Lapusta*, 2009] and the sources of low-frequency earthquakes (LFEs) [e.g., *Nakata et al.*, 2011] that are thought to compose tectonic tremor [e.g., *Shelly et al.*, 2006].

The loading-dependent effects described in this paper suggest that if a fault section is loaded rapidly, it can become orders of magnitude more seismically coupled. Transition zones where tremor has been found to occur may ordinarily slip very slowly and aseismically under slow loading conditions but may become weakly seismic and radiate LFEs/tremor when loaded more rapidly, either from the passage of surface waves from large earthquakes at teleseismic distances (triggered tremor) [e.g., *Gomberg et al.*, 2008] or from slow slip fronts that produce episodic tremor and slip events (ETS) [e.g., *Houston*, 2015; *Wech and Bartlow*, 2014; *Ide*, 2014]. This view of tremor genesis is consistent with the observations of *Wech and Bartlow* [2014] who found a pronounced correlation between slow slip rate and tremor production in Cascadia. These authors also recognized that a single fault section can alternate between tremorgenic and silent [*Wech and Bartlow*, 2014].

Variation in seismic coupling that results from differing loading conditions can also lead to a loading rate dependence on seismically observable M_0 [*Chen et al.*, 2010; *Uchida et al.*, 2015] and stress drop [*McLaskey et al.*, 2012; *Abercrombie*, 2014] as identified by studies of repeating earthquake sequences in response to afterslip. It can also cause these sequences to “shut off” or spontaneously begin as a result of changes in loading characteristics.

7. Conclusions

We have demonstrated that the mode of fault slip can switch between fast/seismic and slow and predominantly aseismic simply as a result of loading conditions. This occurs because the size of the VW fault is close to a critical length scale h^*, and h^* is dependent on loading conditions. The interaction between the VS fault and VW Teflon bearing appears to help facilitate the generation of SSEs, at least compared to a double direct shear configuration that involves the interaction of two VW faults.

We find that long healing times followed by abrupt increases in loading rate act to promote instability, and we interpret this as a reduction in h^* relative to that expected under slow loading. Abrupt increases in loading rate are likely felt by fault sections loaded by an earthquake on a nearby fault (an aftershock) or by the expanding rupture front of an earthquake that nucleated elsewhere or by a slow slip front. In contrast, short healing times and increased loading velocity applied during a postseismic phase can promote stable sliding and a large h^*, which could help explain tremorless slow slip and why stable afterslip can occur on VW fault sections.

In the laboratory, we can generate the full spectrum of slip events ranging from very slow slip events with no detectable seismicity to extremely energetic dynamic stick-slip events that rupture the entire 760 mm long simulated fault in a 2 ms long rupture that radiates seismic waves equivalent to a $M\ -3$ earthquake. In between these two extremes, we observe transitional events that are faintly audible and produce swarms of micro earthquakes ($M\ -6$ to $M\ -8$) with millimeter-sized source dimensions. Despite the continuous spectrum of slip events generated, we observe a distinct change in the seismic coupling that occurs at peak slip rates between 0.03 and 0.07 m/s. Events that slip faster than 0.07 m/s radiate seismic waves that are, in many ways, similar to those of regular earthquakes. Seismic moment is proportional to the total slip which indicates a roughly constant seismic coupling coefficient, and they exhibit a scaling behavior that is similar to laboratory stick-slip behavior reported elsewhere. Slower events exhibit seismic coupling that decreases with decreasing slip speed. This abrupt reduction in seismic coupling at about 0.07 m/s causes events to appear to separate into two distinct categories: slow slip events that are predominantly aseismic and fast stick-slip events that are seismic.

Acknowledgments
Data used in this paper were acquired during laboratory experiments conducted at Cornell University. Data can be made available by the authors upon request. We thank B. Wu, C.-Y. He, and H. Wu for assistance with some of the experiments. We thank D. Lockner and D. Kammer for helpful discussions and T. Bond for technical assistance. We thank C. Marone for a very thorough review that helped improve this paper.

References

Abercrombie, R. E. (2014), Stress drops of repeating earthquakes on the San Andreas fault at Parkfield, *Geophys. Res. Lett.*, *41*, 8784–8791, doi:10.1002/2014GL062079.

Aki, K. (1967), Scaling law of seismic spectrum, *J. Geophys. Res.*, *72*, 1217–1231, doi:10.1029/JZ072i004p01217.

Ampuero, J.-P., and A. M. Rubin (2008), Earthquake nucleation on rate-and-state faults: Aging and slip laws, *J. Geophys. Res.*, *113*, B01302, doi:10.1029/2007JB005082.

Barnhart, W. D., J. R. Murray, R. W. Briggs, F. Gomez, C. P. J. Miles, J. Svarc, S. Riquelme, and B. J. Stressler (2016), Coseismic slip and early afterslip of the 2015 Illapel, Chile, earthquake: Implications for frictional heterogeneity and coastal uplift, *J. Geophys. Res. Solid Earth.*, *121*, 6172–6191, doi:10.1002/2016JB013124.

Baumberger, T., F. Heslot, and B. Perrin (1994), Crossover from creep to inertial motion in friction dynamics, *Nature*, *367*, 544–546.

Bedford, J., et al. (2013), A high-resolution, time-variable afterslip model for the 2010 Maule $M_w = 8.8$, Chile megathrust earthquake, *Earth Planet. Sci. Lett.*, *383*, 26–36, doi:10.1016/j.epsl.2013.09.020.

Ben-David, O., S. M. Rubinstein, and J. Fineberg (2010), Slip-stick and the evolution of frictional strength, *Nature*, *463*, 76–79, doi:10.1038/nature08676.

Blanpied, M. L., D. A. Lockner, and J. D. Byerlee (1995), Frictional slip of granite hydrothermal conditions, *J. Geophys. Res.*, *100*, 13,045–13,064, doi:10.1029/95JB00862.

Boatwright, J., and M. Cocco (1996), Frictional constraints on crustal faulting, *J. Geophys. Res.*, *101*, 13,895–13,909, doi:10.1029/96JB00405.

Brune, J. N. (1970), Tectonic stress and spectra of seismic shear waves from earthquakes, *J. Geophys. Res.*, *75*, 4497–5009, doi:10.1029/JB075i026p04997.

Bürgmann, R., S. Ergintav, P. Segall, E. H. Hearn, S. McClusky, R. Reilinger, H. Woith, and J. Zschau (2002), Time-dependent distributed afterslip on and deep below the Izmit earthquake rupture, *Bull. Seismol. Soc. Am.*, *92*(1), 126–137.

Carpenter, B., M. Ikari, and C. Marone (2016), Laboratory observations of time-dependent frictional strengthening and stress relaxation in natural and synthetic fault gouges, *J. Geophys. Res. Solid Earth*, *121*, 1183–1201, doi:10.1002/2015JB012136.

Chang, J. C., D. A. Lockner, and Z. Reches (2012), Rapid acceleration leads to rapid weakening in earthquake-like laboratory experiments, *Science*, *338*, 101–105.

Chen, K. H., R. Burgmann, R. M. Nadeau, T. Chen, and N. Lapusta (2010), Postseismic variations in seismic moment and recurrence interval of repeating earthquakes, *Earth Planet. Sci. Lett.*, *299*, 118–125.

Chen, T., and N. Lapusta (2009), Scaling of small repeating earthquakes explained by interaction of seismic and aseismic slip in a rate and state fault model, *J. Geophys. Res.*, *113*, B01311, doi:10.1029/2008JB005749.

Collettini, C., G. Di Stefano, B. M. Carpenter, P. Scarlato, T. Tesei, S. Mollo, F. Trippetta, C. Marone, G. Romeo, and L. Chiaraluce (2014), A novel and versatile apparatus for brittle rock deformation, *Int. J. Rock Mech. Min.*, *66*.

Dieterich, J. H. (1978), Time-dependent friction and the mechanics of stick-slip, *Pure Appl. Geophys.*, *116*, 790–806.

Dieterich, J. H. (1979), Modeling of rock friction: 1. Experimental results and constitutive equations, *J. Geophys. Res.*, *84*, 2161–2168, doi:10.1029/JB084iB05p02161.

Dieterich, J. H. (1992), Earthquake nucleation on faults with rate- and state-dependent friction, *Tectonophysics*, *211*, 115–134.

Dieterich, J. H., and B. D. Kilgore (1994), Direct observation of frictional contacts: New insights for state-dependent properties, *Pure Appl. Geophys.*, *143*, 283–302.

Floyd, M. A., et al. (2016), Spatial variations in fault friction related to lithology from rupture and afterslip of the 2014 South Napa, California, earthquake, *Geophys. Res. Lett.*, *43*, 6808–6816, doi:10.1002/2016GL069428.

Fang, Z., J. H. Dieterich, and G. Xu (2010), Effect of initial conditions and loading path on earthquake nucleation, *J. Geophys. Res.*, *115*, B06313, doi:10.1029/2009JB006558.

Frankel, A., and H. Kanamori (1983), Determination of rupture duration and stress drop from earthquakes in Southern California, *Bull. Seismol. Soc. Am.*, *73*, 1527–1551.

Fukuyama, E., et al. (2014), Large-scale biaxial friction experiments using a NIED large-scale shaking table—Design of apparatus and preliminary results, *Rep. Natl. Res. Inst. Earth Sci. Disaster Prev.*, *81*, 15–35.

Gomberg, J., J. L. Rubinstein, Z. Peng, K. C. Creager, and J. E. Vidale (2008), Widespread triggering of non-volcanic tremor in California, *Science*, *319*, 173, doi:10.1126/science.1149164.

Gu, J.-C., J. R. Rice, A. L. Ruina, and S. T. Tse (1984), Slip motion and stability of a single degree of freedom elastic system with rate and state dependent friction, *J. Mech. Phys. Solids*, *32*, 167–196.

Gu, Y., and T.-F. Wong (1994), Non-linear dynamics of the transition from stable sliding to cyclic stick-slip in rock, in *Nonlinear Dynamics and Predictability of Geophysical Phenomena*, *Geophys. Monogr. Ser.*, vol. 83, edited by W. I. Newman, A. Gabrielov, and D. L. Turcotte, pp. 15–35, AGU, Washington, D. C.

Helmstetter, A., and B. E. Shaw (2009), Afterslip and aftershocks in the rate-and-state friction law, *J. Geophys. Res.*, *114*, B01308, doi:10.1029/2007JB005077.

Hough, S. E., and D. S. Dreger (1995), Source parameters of the 23 April 1992 *M* 6.1 Joshua Tree, California, earthquake and its aftershocks: Empirical Green's function analysis of GEOS and TERRA scope data, *Bull. Seismol. Soc. Am.*, *85*, 1576–1590.

Houston, H. (2015), Low friction and fault weakening revealed by rising sensitivity of tremor to tidal stress, *Nat. Geosci.*, *8*, 409–415, doi:10.1038/ngeo2419.

Hutchings, W., and F. Wu (1990), Empirical Green's functions from small earthquakes: A waveform study of locally recorded aftershocks of the 1971 San Fernando earthquake, *J. Geophys. Res.*, *95*, 1187–1214.

Ide, S. (2014), Modeling fast and slow earthquakes at various scales, *Proc. Jpn. Acad., Ser. B*, *90*(8), 259–277, doi:10.2183/pjab.90.259.

Ikari, M., C. Marone, and D. Saffer (2011), On the relation between fault strength of frictional stability, *Geology*, *39*, 83–86.

Ito, Y., et al. (2013), Episodic slow slip events in the Japan subduction zone before the 2011 Tohoku-Oki earthquake, *Tectonophysics*, *600*, 14–26, doi:10.1016/j.tecto.2012.08.022.

Johnson, K. M., J. I. Fukuda, and P. Segall (2012), Challenging the rate-state asperity model: Afterslip following the 2011 *M*9 Tohoku-oki, Japan, earthquake, *Geophys. Res. Lett.*, *39*, L20302, doi:10.1029/2012GL052901.

Johnson, K. M., A. Mavrommatis, and P. Segall (2016), Small interseismic asperities and widespread aseismic creep on the northern Japan subduction interface, *Geophys. Res. Lett.*, *43*, 135–143, doi:10.1002/2015GL066707.

Johnson, T. L., and C. H. Scholz (1976), Dynamic properties of stick-slip friction of rock, *J. Geophys. Res.*, *81*(5), 881–888, doi:10.1029/JB081i005p00881.

Kammer, D. S., M. Radiguet, J.-P. Ampuero, and J.-F. Molinari (2015), Linear elastic fracture mechanics predicts the propagation distance of frictional slip, *Tribol. Lett.*, *57*, 23, doi:10.1007/s11249-014-0451-8.

Kaneko, Y., and N. Lapusta (2008), Variability of earthquake nucleation in continuum models of rate-and-state faults and implications for aftershock rates, *J. Geophys. Res.*, *113*, B12312, doi:10.1029/2007JB005154.

Kaneko, Y., S. B. Nielsen, and B. M. Carpenter (2016), The onset of laboratory earthquakes explained by nucleating rupture on a rate-and-state fault, *J. Geophys. Res. Solid Earth*, *121*, 6071–6091, doi:10.1002/2016JB013143.

Kaproth, B., and C. Marone (2013), Slow earthquakes, preseismic velocity changes, and the origin of slow frictional stick-slip, *Science*, *341*, 1229.

Karner, S. L., and Marone, C. (2000), Effects of loading rate and normal stress on stress drop and stick-slip recurrence interval, in *Geocomplexity and the Physics of Earthquakes*, *Geophys. Monogr. Ser.*, vol. 120, edited by J. B. Rundle, D. Turcotte, and W. Klein, pp. 187–198, AGU, Washington, D. C.

Kato, N., K. Yamamoto, H. Yamamoto, and T. Hirasawa (1992), Strain-rate effect on frictional strength and the slip nucleation process, *Tectonophysics*, *211*(1), 269–282.

Kilgore, B. D., A. McGarr, N. M. Beeler, and D. A. Lockner (2017), Earthquake source properties from instrumented laboratory stick-slip, in *Fault Zone Dynamic Processes: Evolution of Fault Properties During Seismic Rupture*, edited by M. Thomas, H. Bhat, and T. Mitchell, pp. 150–169, AGU, Washington, D. C. [Available at http://www.wiley.com/WileyCDA/WileyTitle/productCd-1119156882.html.]

Latour, S., A. Schubnel, S. Nielsen, R. Madariaga, and S. Vinciguerra (2013), Characterization of nucleation during laboratory earthquakes, *Geophys. Res. Lett.*, *40*, 5064–5069, doi:10.1002/grl.50974.

Leeman, J. R., D. M. Saffer, M. M. Scuderi, and C. Marone (2016), Laboratory observations of slow earthquakes and the spectrum of tectonic fault slip modes, *Nat. Commun.*, *7*, 1–6, doi:10.1038/ncomms11104.

Lin, Y. N., et al. (2013), Coseismic and postseismic slip associated with the 2010 Maule earthquake, Chile: Characterizing the Arauco Peninsula barrier effect, *J. Geophys. Res. Solid Earth*, *118*, 3142–3159, doi:10.1002/jgrb.50207.

Liu, Y., and J. R. Rice (2005), Aseismic slip transients emerge spontaneously in three-dimensional rate and state modeling of subduction earthquake sequences, *J. Geophys. Res.*, *110*, B08307, doi:10.1029/2004JB003424.

Liu, Y., and J. R. Rice (2007), Spontaneous and triggered aseismic deformation transients in a subduction fault model, *J. Geophys. Res.*, *112*, B09404, doi:10.1029/2007JB004930.

Lui, S. K. Y., and Lapusta, N. (2016), Repeating microearthquake sequences interact predominantly through postseismic slip, *Nat. Commun.*, *7*, 13020, doi:10.1038/ncomms13020.

Marone, C. (1998), Laboratory-derived friction laws and their application to seismic faulting, *Annu. Rev. Earth Planet. Sci.*, *26*, 643–696, doi:10.1146/annurev.earth.26.1.643.

Marone, C., J. Vidale, and W. Ellsworth (1995), Fault healing inferred from time dependent variations in source properties of repeating earthquakes, *Geophys. Res. Lett.*, *22*, 3095–3098.

McLaskey, G. C., and B. D. Kilgore (2013), Foreshocks during the nucleation of stick-slip instability, *J. Geophys. Res. Solid Earth*, *118*, 2982–2997, doi:10.1002/jgrb.50232.

McLaskey, G. C., and D. A. Lockner (2014), Preslip and cascade processes initiating laboratory stick–slip, *J. Geophys. Res. Solid Earth*, *119*, 6323–6336, doi:10.1002/2014JB011220.

McLaskey, G. C., A. M. Thomas, S. D. Glaser, and R. M. Nadeau (2012), Fault healing promotes high frequency earthquakes in laboratory experiments and on natural faults, *Nature*, *491*, 101–104.

McLaskey, G. C., B. D. Kilgore, D. A. Lockner, and N. M. Beeler (2014), Laboratory generated **M** -6 earthquakes, *Pure Appl. Geophys.*, *171*(10), 2601–2615, doi:10.1007/s00024-013-0772-9.

McLaskey, G. C., D. A. Lockner, B. D. Kilgore, and N. M. Beeler (2015), A robust calibration technique for acoustic emission systems based on momentum transfer from a ball drop, *Bull. Seismol. Soc. Am.*, *105*(1), 257–271, doi:10.1785/0120140170.

McGarr, A. (2012), Relating stick-slip friction experiments to earthquake source parameters, *Geophys. Res. Lett.*, *39*, L05303, doi:10.1029/2011GL050327.

Mokha, A., M. Constantinou, and A. Reinhorn (1990), Teflon bearings in base isolation I: Testing, *J. Struct. Eng.*, *116*(2), 438–454.

Mueller, C. S. (1985), Source pulse enhancement by deconvolution of an empirical Green's function, *Geophys. Res. Lett.*, *12*, 33–36, doi:10.1029/GL012i001p00033.

Nakata, R., R. Ando, T. Hori, and S. Ide (2011), Generation mechanism of slow earthquakes: Numerical analysis based on a dynamic model with brittle-ductile mixed fault heterogeneity, *J. Geophys. Res.*, *116*, B08308, doi:10.1029/2010JB008188.

Nielsen, S., J. Taddeucci, and S. Vinciguerra (2010), Experimental observation of stick-slip instability fronts, *Geophys. J. Int.*, *180*, 697–702, doi:10.1111/j.1365-246X.2009.0444.x.

Noda, H., and N. Lapusta (2013), Stable creeping fault segments can become destructive as a result of dynamic weakening, *Nature*, *493*(7433), 518–521.
Ohnaka, M., and Y. Kuwahara (1990), Characteristic features of local breakdown near a crack-tip in the transition zone from nucleation to unstable rupture during stick-slip shear failure, *Tectonophysics*, *175*(1), 197–220.
Ohnaka, M., and L. F. Shen (1999), Scaling of the shear rupture process from nucleation to dynamic propagation: Implications of geometric irregularity of the rupturing surfaces, *J. Geophys. Res.*, *104*, 817–844, doi:10.1029/1998JB900007.
Okazaki, K., and I. Katayama (2015), Slow stick slip of antigorite serpentinite under hydrothermal conditions as a possible mechanism for slow earthquakes, *Geophys. Res. Lett.*, *42*, 1099–1104, doi:10.1002/2014GL062735.
Okubo, P. G., and J. H. Dieterich (1984), Effects of physical fault properties on frictional instabilities produced on simulated faults, *J. Geophys. Res.*, *89*(B7), 5817–5827, doi:10.1029/JB089iB07p05817.
Perfettini, H., and J. P. Avouac (2014), The seismic cycle in the area of the 2011 M_w9.0 Tohoku-Oki earthquake, *J. Geophys. Res. Solid Earth*, *119*, 4469–4515, doi:10.1002/2013JB010697.
Pritchard, M. E., and M. Simons (2006), An aseismic slip pulse in northern Chile and along-strike variations in seismogenic behavior, *J. Geophys. Res.*, *111*, B08405, doi:10.1029/2006JB004258.
Rice, J. R. (2006), Heating and weakening of faults during earthquake slip, *J. Geophys. Res.*, *111*, B05311, doi:10.1029/2005JB004006.
Rice, J. R., and J.-C. Gu (1983), Earthquake aftereffects and triggered seismic phenomena, *Pure Appl. Geophys.*, *121*, 187–219.
Rice, J. R., and A. L. Ruina (1983), Stability of steady frictional sliding, *J. Appl. Mech.*, *50*, 343–349.
Rosakis, A. J., H. Kanamori, and K. Xia (2006), Laboratory earthquakes, *Int. J. Fract.*, *138*, 211–218.
Rubin, A. M., and J.-P. Ampuero (2005), Earthquake nucleation on (aging) rate and state faults, *J. Geophys. Res.*, *110*, B11312, doi:10.1029/2005JB003686.
Ruina, A. (1983), Slip instability and state variable friction laws, *J. Geophys. Res.*, *88*, 10,359–10,370, doi:10.1029/JB088iB12p10359.
Selvadurai, P., and S. Glaser (2017), Asperity generation and its relationship to seismicity on a planar fault: A laboratory simulation, *Geophys. J. Int.*, *208*(2), 1009–1025.
Selvadurai, P. A., and S. D. Glaser (2015), Laboratory developed contact models controlling instability on frictional faults, *J. Geophys. Res. Solid Earth*, *120*, 4208–4236, doi:10.1002/2014JB011690.
Scholz, C., P. Molnar, and T. Johnson (1972), Detailed studies of frictional sliding of granite and implications for the earthquake mechanism, *J. Geophys. Res.*, *77*, 6392–6406, doi:10.1029/JB077i032p06392.
Segall, P., A. M. Rubin, A. M. Bradley, and J. R. Rice (2010), Dilatant strengthening as a mechanism for slow slip events, *J. Geophys. Res.*, *115*, B12305, doi:10.1029/2010JB007449.
Shelly, D. R. (2010), Periodic, chaotic, and doubled earthquake recurrence intervals on the deep San Andreas fault, *Science*, *328*, 1385, doi:10.1126/science.1189741.
Shelly, D. R., G. C. Beroza, S. Ide, and S. Nakamula (2006), Low-frequency earthquakes in shikoku, Japan, and their relationship to episodic tremor and slip, *Nature*, *442*(7099), 188–191.
Skarbek, R., A. Rempel, and D. Schmidt (2012), Geologic heterogeneity can produce aseismic slip transients, *Geophys. Res. Lett.*, *39*, L21306, doi:10.1029/2012GL053762.
Tanikawa, W., and T. Shimamoto (2009), Frictional and transport properties of the Chelungpu fault from shallow borehole data and their correlation with seismic behavior during the 1999 Chi-Chi earthquake, *J. Geophys. Res.*, *114*, B01502, doi:10.1029/2008JB005750.
Tinti, E., M. M. Scuderi, L. Scognamiglio, G. Di Stefano, C. Marone, and C. Collettini (2016), On the evolution of elastic properties during laboratory stick-slip experiments spanning the transition from slow slip to dynamic rupture, *J. Geophys. Res. Solid Earth*, *121*, 8569–8594, doi:10.1002/2016JB013545.
Togo, T., T. Shimamoto, F. Yamashita, E. Fukuyama, K. Mizoguchi, and Y. Urata (2015), *Earthquake Sci.*, *28*, 97–118, doi:10.1007/s11589-015-0113-4.
Uchida, N., and T. Matsuzawa (2013), Pre- and postseismic slow slip surrounding the 2011 Tohoku-oki earthquake rupture, *Earth Planet. Sci. Lett.*, *374*, 81–91.
Uchida, N., S. Shimamura, T. Matsuzawa, and T. Okada (2015), Postseismic response of repeating earthquakes around the 2011 Tohoku-oki earthquake: Moment increases due to the fast loading rate, *J. Geophys. Res. Solid Earth*, *120*, 259–274, doi:10.1002/2013JB010933.
Vidale, J., W. Ellsworth, A. Cole, and C. Marone (1994), Varions in rupture process with recurrence interval in a repeated small earthquake, *Nature*, *368*, 624–626.
Veedu, D. M., and S. Barbot (2016), The Parkfield tremors reveal slow and fast ruptures on the same asperity, *Nature*, *532*, 361–365, doi:10.1038/nature17190.
Voisin, C., F. Renard, and J.-R. Grasso (2007), Long term friction: From stick-slip to stable sliding, *Geophys. Res. Lett.*, *34*, L13301, doi:10.1029/2007GL029715.
Walter, B. R., Mayeda, K., and Gok, R. (2006), *Earthquakes: Radiated Energy and the Physics of Earthquake Faulting*, *Geophys. Monogr. Ser.*, vol. 170, edited by R. Abercrombie et al., pp. 25–41, AGU, Washington, D. C.
Wech, A. G., and N. M. Bartlow (2014), Slip rate and tremor genesis in Cascadia, *Geophys. Res. Lett.*, *41*, 392–398, doi:10.1002/2013GL058607.
Wei, M., Y. Kaneko, Y. Liu, and J. J. McGuire (2013), Episodic fault creep events in California controlled by shallow frictional heterogeneity, *Nat. Geosci.*, *6*, 566–570, doi:10.1038/ngeo1835.